Metrol. Meas. Syst., Vol. XXII (2015), No. 1, pp. 51–68.

PAN POLSKA AKADEMIA NAUK

METROLOGY AND MEASUREMENT SYSTEMS

Index 330930, ISSN 0860-8229

www.metrology.pg.gda.pl

M&MS

THE STATIC UNBALANCE ANALYSIS AND ITS MEASUREMENT SYSTEM FOR GIMBALS AXES OF AN INERTIAL STABILIZATION PLATFORM

Hui Yang, Yan Zhao, Min Li, Falin Wu

School of Instrumentation Science and Opto-electronics Engineering, Beihang University, Beijing 100191, China
(✉falin.wu@buaa.edu.cn, +86 10 82313929)

Abstract

To reduce the influence of the static unbalance on an infrared missile guidance system, a new static unbalance measure system for the gimbals axes has been developed. Considering the coupling effects caused by a mass eccentricity, the static balance condition and measure sequence for each gimbal axis are obtained. A novel static unbalance test approach is proposed after analyzing the dynamic model of the measured gimbal axis. This approach is to drive the measured gimbal axis to do sinusoidal reciprocating motion in a small angle and collect its drive currents in real time. Then the static unbalance of the measured gimbal axis can be obtained by the current multi-cycle integration. Also a measuring system using the proposed approach has been developed. A balanced simulator is used to verify the proposed approach by the load and repeatability tests. The results show the proposed approach enhances the efficiency of the static unbalance measurement, and the developed measuring system is able to achieve a high precision with a greater stability.

Keywords: inertial stabilization platform, mass eccentricity, angular position turntable, dynamical model, least-square fitting.

1. Introduction

An inertial stabilization platform is the core component of an infrared guidance system, which generally is composed of a mechanical device, tri-axial gimbals, torque motors, sensors, information processing circuits and other units. The aim of an inertial stabilization platform is to stabilize the sensor's line of sight towards a target by isolating the sensor from the disturbance induced by the operating environment, such as various disturbance torques and body motions [1–4]. In an inertial stabilization platform, because of the structure design errors, material defects, machining and assembly errors, and so on, the centroid is usually shifted from the center of a gimbals axis, which causes an unbalance torque. Furthermore, the unbalance torque will be increased with the augment of the carrier acceleration. As a result of the coupling effect between the gimbals elements, once the unbalance torque is beyond a certain level, not only the optical axis vibrations and the output signals unsteadiness will be induced, but also the hit accuracy and the flight stability of a missile will be attenuated [5-6]. In order to improve the missile guidance accuracy and reliability, and reduce the power consumption due to the appearance of the static unbalance torque during the adjustment process, the mass eccentricity of the gimbals axes must be calibrated. Therefore, it is important to analyse the static unbalance property of the inertial stabilization platform and find an appropriate method to test the static unbalance.

In the past decades, two typical categories of test systems based on the principle of hydrostatic supporting or optical adjusting, respectively, have been developed to measure the rotor static unbalance [7–12]. Such methods as the electronic balance, guide rolling and the

Article history: received on May. 09, 2014; accepted on Sep. 22, 2014; available online on Mar. 15, 2015; DOI: 10.1515/mms-2015-0002.

multipoint measurement fall into the first category, which is based on the principle of hydrostatic supporting. Although the realization of the first category methods is fairly simple, the measuring systems corresponding with them are usually purely mechanical systems which are difficult to install or dismantle. Thus, the first category methods are inconvenient to use and have a low testing precision. The second category methods mainly use the optical adjustment approach. They overcome the inconveniences of the first category methods. However, they often encounter the problem of a poor stability and a low efficiency, since they rely more on environment changes. In order to overcome the shortcomings of the conventional methods, an influence coefficient method and a modal balance method have been investigated in recent years. Several rotor vibration types can be balanced at the same time by using the influence coefficient method. With the aid of a computer, this method can easily achieve the balance and automation of data processing. However, using this method may cause many balance reboots at a high rotation speed, and the sensitivity will be reduced in the case of balancing a higher vibration type [13–15]. On the contrary, by using the modal balance method to balance the rotor fewer balance reboots occur at a high rotation speed, and this method has a higher sensitivity even at a lower order vibration type. But, when the system damping impact increases, this method may encounter a problem of difficult determining a certain vibration type, so its availability is reduced [16–18]. A much more serious inconvenience of both the influence coefficient and the modal balance methods is consuming much more time to deal with rather complex calculations. The two methods apply many fixtures to fix the measured object, and the rotation speed is difficult to control effectively, which could easily damage a measured object. Therefore, they are not appropriate for balancing a precision equipment.

To improve the tracking accuracy of an infrared missile guidance system, the static unbalance torque caused by the mass eccentricity of gimbals axes must be reduced. Because the above mentioned methods and systems are not suitable to test the unbalance of gimbals axes for the inertial stabilization platform, this paper proposes a new unbalance testing method of gimbals axes and a design of a new measuring system. First, the coupling effect caused by the static unbalance between the gimbals elements of the inertial platform is analysed. Then, a current integration method used to test the unbalance of a gimbals axis is proposed, followed by the development of a test system based on the proposed method. Finally, a balanced simulator of the inertial stabilization platform is used to conduct loading tests and repeatability tests. The results prove the effectiveness of the proposed test method and the developed measuring system.

2. The static balance analysis of the inertial platform gimbals axes

The structure of the inertial stabilization platform is shown in Fig. 1. It contains three gimbals; each for one degree of freedom. From now on they will be called the outer, the middle and the inner gimbal. The outer gimbal is the carrier of the middle gimbal axis, and its axis is placed on the base. The optical detector is fixed on the inner gimbal, and the inner gimbal axis is fixed on the middle gimbal. The outer, middle and inner gimbal axes are perpendicular to each other. This structure not only isolates interferences from the carrier itself and from other external disturbances, but also assures the optical axis of the detector precisely pointing at the target while the gimbals are in the continual regulation[19]. To facilitate modelling and analyzing the coupling effect caused by the mass eccentricity of gimbal axes, five coordinates are defined in this study, and the relationships between them are shown in Fig. 2. It is assumed that the coordinate $o_g x_g y_g z_g$ is the inertial coordinate system, and the coordinate $o_b x_b y_b z_b$ is the base coordinate system which is used to describe the motion of the carrier. The coordinate $o_g x_g y_g z_g$ and $o_{\mathrm{b}} x_{\mathrm{b}} y_{\mathrm{b}} z_{\mathrm{b}}$ coincide with each other while

the carrier is static. The coordinate $o_{\mathrm{o}}x_{\mathrm{o}}y_{\mathrm{o}}z_{\mathrm{o}}$ is fixed to the outer gimbal. The angle of rotation α is defined as a positive angle of rotation around the x_{b}, and the matrix $\boldsymbol{C}_{\mathrm{b}}^{\mathrm{o}}$ depicts the transformation from $o_{\mathrm{b}}x_{\mathrm{b}}y_{\mathrm{b}}z_{\mathrm{b}}$ to $o_{\mathrm{o}}x_{\mathrm{o}}y_{\mathrm{o}}z_{\mathrm{o}}$. The coordinate $o_{\mathrm{m}}x_{\mathrm{m}}y_{\mathrm{m}}z_{\mathrm{m}}$ is fixed to the middle gimbal. The angle of rotation β is defined as a positive angle of rotation around the z_{o}, and the matrix $\boldsymbol{C}_{\mathrm{o}}^{\mathrm{m}}$ depicts the transformation from $o_{\mathrm{o}}x_{\mathrm{o}}y_{\mathrm{o}}z_{\mathrm{o}}$ to $o_{\mathrm{m}}x_{\mathrm{m}}y_{\mathrm{m}}z_{\mathrm{m}}$. The coordinate $o_{\mathrm{p}}x_{\mathrm{p}}y_{\mathrm{p}}z_{\mathrm{p}}$ is fixed to the inner gimbal. The angle of rotation γ is defined as a positive angle of rotation around the y_{m}, and the matrix $\boldsymbol{C}_{\mathrm{m}}^{\mathrm{p}}$ describes the transformation from $o_{\mathrm{m}}x_{\mathrm{m}}y_{\mathrm{m}}z_{\mathrm{m}}$ to $o_{\mathrm{p}}x_{\mathrm{p}}y_{\mathrm{p}}z_{\mathrm{p}}$. In the case of the initial condition, the flats of the middle gimbal and the inner gimbal coincide with each other. The optical detector is fixed on the inner gimbal and its axis is exactly aligned with $o_{\mathrm{p}}x_{\mathrm{p}}$; they are pointing at the front of the carrier.

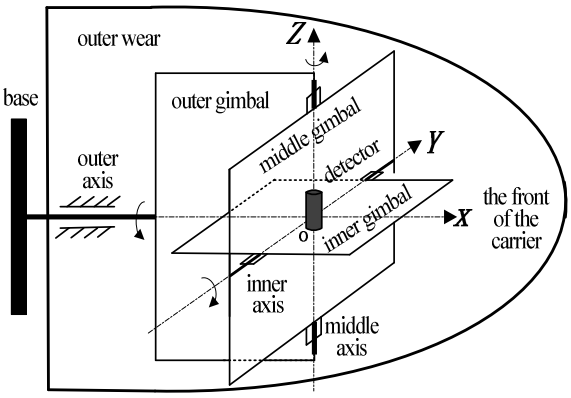

Fig. 1. The structure of the inertial stabilization platform.

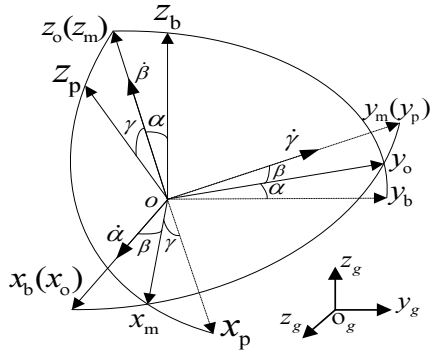

Fig. 2. Relationships between coordinates.

According to the coordinates $o_{\mathrm{o}}x_{\mathrm{o}}y_{\mathrm{o}}z_{\mathrm{o}}$, $o_{\mathrm{m}}x_{\mathrm{m}}y_{\mathrm{m}}z_{\mathrm{m}}$ and $o_{\mathrm{p}}x_{\mathrm{p}}y_{\mathrm{p}}z_{\mathrm{p}}$ defined above, the gravitational acceleration of the inertial stabilization platform is described from the inertial coordinate to the outer, middle and inner coordinates, respectively, as follows:

$$\boldsymbol{g}_{\mathrm{o}} = \begin{bmatrix} g_{\mathrm{ox}} \\ g_{\mathrm{oy}} \\ g_{\mathrm{oz}} \end{bmatrix} = \boldsymbol{C}_{\mathrm{b}}^{\mathrm{o}} \begin{bmatrix} 0 \\ 0 \\ -g \end{bmatrix} = \begin{bmatrix} 0 \\ -\sin\alpha \\ -\cos\alpha \end{bmatrix} g \ , \tag{1}$$

$$\boldsymbol{g}_{\mathrm{m}} = \begin{bmatrix} g_{\mathrm{mx}} \\ g_{\mathrm{mx}} \\ g_{\mathrm{mx}} \end{bmatrix} = \boldsymbol{C}_{\mathrm{o}}^{\mathrm{m}} \boldsymbol{C}_{\mathrm{b}}^{\mathrm{o}} \begin{bmatrix} 0 \\ 0 \\ -g \end{bmatrix} = \begin{bmatrix} -\sin\alpha\sin\beta \\ -\sin\alpha\cos\beta \\ -\cos\alpha \end{bmatrix} g \ , \tag{2}$$

$$\boldsymbol{g}_{\mathrm{p}} = \begin{bmatrix} g_{\mathrm{px}} \\ g_{\mathrm{py}} \\ g_{\mathrm{pz}} \end{bmatrix} = \boldsymbol{C}_{\mathrm{m}}^{\mathrm{p}} \boldsymbol{C}_{\mathrm{o}}^{\mathrm{m}} \boldsymbol{C}_{\mathrm{b}}^{\mathrm{o}} \begin{bmatrix} 0 \\ 0 \\ -g \end{bmatrix} = \begin{bmatrix} -\sin\alpha\sin\beta\cos\gamma + \cos\alpha\sin\gamma \\ -\sin\alpha\cos\beta \\ -\sin\alpha\sin\beta\sin\gamma - \cos\alpha\cos\gamma \end{bmatrix} g \ . \tag{3}$$

It is assumed that the gimbals and the detector are rigid bodies, and only relative rotations exist between each of the gimbals. The symbols m_{p}, m_{m} and m_{o} represent masses of the inner, middle and outer gimbals, respectively. The centroids of each gimbal will not be in the origin after some adjustment has been made to the inertial stabilization platform, so they are described in their coordinates as $\boldsymbol{r}_{\mathrm{p}} = (x_{\mathrm{p}}, y_{\mathrm{p}}, z_{\mathrm{p}})^{\mathrm{T}}$, $\boldsymbol{r}_{\mathrm{m}} = (x_{\mathrm{m}}, y_{\mathrm{m}}, z_{\mathrm{m}})^{\mathrm{T}}$ and $\boldsymbol{r}_{\mathrm{o}} = (x_{\mathrm{o}}, y_{\mathrm{o}}, z_{\mathrm{o}})^{\mathrm{T}}$, respectively.

In the inner gimbal coordinate, the unbalance torque projects in $o_{\mathrm{p}}x_{\mathrm{p}}y_{\mathrm{p}}z_{\mathrm{p}}$ can be expressed by $\boldsymbol{M}_{\mathrm{p}}$, which is caused by the mass eccentricity of the inner gimbal and its load.

$$\begin{aligned}\boldsymbol{M}_{\mathrm{p}} &= \begin{bmatrix} M_{\mathrm{px}} & M_{\mathrm{py}} & M_{\mathrm{pz}} \end{bmatrix}^{\mathrm{T}} \\ &= m_{\mathrm{p}}\left[\tilde{g}_{\mathrm{p}}\right]\begin{bmatrix} x_{\mathrm{p}} & y_{\mathrm{p}} & z_{\mathrm{p}} \end{bmatrix}^{\mathrm{T}} \\ &= \begin{bmatrix} m_{\mathrm{p}}gy_{\mathrm{p}}\sin\alpha\sin\beta\sin\gamma + m_{\mathrm{p}}gy_{\mathrm{p}}\cos\alpha\cos\gamma - m_{\mathrm{p}}gz_{\mathrm{p}}\sin\alpha\cos\beta \\ -m_{\mathrm{p}}gx_{\mathrm{p}}\sin\alpha\sin\beta\sin\gamma - m_{\mathrm{p}}gx_{\mathrm{p}}\cos\alpha\cos\gamma + m_{\mathrm{p}}gz_{\mathrm{p}}\sin\alpha\sin\beta\cos\gamma - m_{\mathrm{p}}gz_{\mathrm{p}}\cos\alpha\sin\gamma \\ m_{\mathrm{p}}gx_{\mathrm{p}}\sin\alpha\cos\beta - m_{\mathrm{p}}gy_{\mathrm{p}}\sin\alpha\sin\beta\cos\gamma + m_{\mathrm{p}}gy_{\mathrm{p}}\cos\alpha\sin\gamma \end{bmatrix}\end{aligned}, \tag{4}$$

where $\left[\tilde{g}_{\mathrm{p}}\right]$ denotes the anti-symmetric matrix of vector $\boldsymbol{g}_{\mathrm{p}}$ in $o_{\mathrm{p}}x_{\mathrm{p}}y_{\mathrm{p}}z_{\mathrm{p}}$.

Since the inner gimbal can only rotate around y_p and the unbalance torque of the inner gimbal is only generated along y_p, the static balance condition for the inner gimbal is $M_{\mathrm{py}} = 0$, i.e.

$$-m_{\mathrm{p}}gx_{\mathrm{p}}\sin\alpha\sin\beta\sin\gamma - m_{\mathrm{p}}gx_{\mathrm{p}}\cos\alpha\cos\gamma + m_{\mathrm{p}}gz_{\mathrm{p}}\sin\alpha\sin\beta\cos\gamma - m_{\mathrm{p}}gz_{\mathrm{p}}\cos\alpha\sin\gamma = 0. \tag{5}$$

It is obvious that α, β, γ change with time. So, to make the Eq. (5) true, it requires holding the following Eq. (6):

$$\begin{cases} x_{\mathrm{p}} = 0 \\ z_{\mathrm{p}} = 0 \end{cases}. \tag{6}$$

Similarly, the unbalance torque projects in $o_{\mathrm{m}}x_{\mathrm{m}}y_{\mathrm{m}}z_{\mathrm{m}}$ can be expressed by $\boldsymbol{M}_m$, which is caused by the mass eccentricity of the middle gimbal and its load.

$$\begin{aligned}\boldsymbol{M}_{\mathrm{m}} &= \begin{bmatrix} M_{\mathrm{mx}} & M_{\mathrm{my}} & M_{\mathrm{mz}} \end{bmatrix}^{\mathrm{T}} \\ &= m_{\mathrm{m}}\left[\tilde{g}_{\mathrm{m}}\right]\begin{bmatrix} x_{\mathrm{m}} & y_{\mathrm{m}} & z_{\mathrm{m}} \end{bmatrix}^{\mathrm{T}} + m_{\mathrm{p}}\left[\tilde{g}_{\mathrm{m}}\right]\left(C_{\mathrm{m}}^{\mathrm{p}}\right)^{-1}\begin{bmatrix} x_{\mathrm{p}} & y_{\mathrm{p}} & z_{\mathrm{p}} \end{bmatrix}^{\mathrm{T}} \\ &= \begin{bmatrix} m_{\mathrm{m}}gy_{\mathrm{m}}\cos\alpha - m_{\mathrm{m}}gz_{\mathrm{m}}\sin\alpha\cos\beta + m_{\mathrm{p}}gx_{\mathrm{p}}\sin\alpha\cos\beta\sin\gamma + m_{\mathrm{p}}gy_{\mathrm{p}}\cos\alpha - m_{\mathrm{p}}gz_{\mathrm{p}}\sin\alpha\cos\beta\cos\gamma \\ -m_{\mathrm{m}}gx_{\mathrm{m}}\cos\alpha + m_{\mathrm{m}}gz_{\mathrm{m}}\sin\alpha\sin\beta - m_{\mathrm{p}}gx_{\mathrm{p}}\cos\alpha\cos\gamma - m_{\mathrm{p}}gx_{\mathrm{p}}\sin\alpha\sin\beta\sin\gamma - m_{\mathrm{p}}gz_{\mathrm{p}}\cos\alpha\sin\gamma + m_{\mathrm{p}}gz_{\mathrm{p}}\sin\alpha\sin\beta\cos\gamma \\ m_{\mathrm{m}}gx_{\mathrm{m}}\sin\alpha\cos\beta - m_{\mathrm{m}}gy_{\mathrm{m}}\sin\alpha\sin\beta + m_{\mathrm{p}}gx_{\mathrm{p}}\sin\alpha\cos\beta\cos\gamma - m_{\mathrm{p}}gy_{\mathrm{p}}\sin\alpha\sin\beta + m_{\mathrm{p}}gz_{\mathrm{p}}\sin\alpha\cos\beta\sin\gamma \end{bmatrix}\end{aligned}, \tag{7}$$

where $\left[\tilde{g}_{\mathrm{m}}\right]$ denotes the anti-symmetric matrix of vector $\boldsymbol{g}_{\mathrm{m}}$ in $o_{\mathrm{m}}x_{\mathrm{m}}y_{\mathrm{m}}z_{\mathrm{m}}$.

Because the middle gimbal rotates only around z_m, and the unbalance torque of the middle gimbal exists only along z_m, the static balance condition for the middle gimbal is $M_{\mathrm{mz}} = 0$, i.e.

$$\begin{aligned} m_{\mathrm{m}}gx_{\mathrm{m}}\sin\alpha\cos\beta - m_{\mathrm{m}}gy_{\mathrm{m}}\sin\alpha\sin\beta + m_{\mathrm{p}}gx_{\mathrm{p}}\sin\alpha\cos\beta\cos\gamma \\ - m_{\mathrm{p}}gy_{\mathrm{p}}\sin\alpha\sin\beta + m_{\mathrm{p}}gz_{\mathrm{p}}\sin\alpha\cos\beta\sin\gamma = 0. \end{aligned}. \tag{8}$$

Since α, β, γ change with time, only the condition of the Eq. (9) is satisfied. So, the Eq. (8) can be true.

$$\begin{cases} x_{\mathrm{p}} = 0 \\ z_{\mathrm{p}} = 0 \\ x_{\mathrm{m}} = 0 \\ m_{\mathrm{m}} y_{\mathrm{m}} + m_{\mathrm{p}} y_{\mathrm{p}} = 0 \end{cases}. \tag{9}$$

In addition, the unbalance torque projects in $o_{\mathrm{o}}x_{\mathrm{o}}y_{\mathrm{o}}z_{\mathrm{o}}$ can be expressed by $\boldsymbol{M}_o$, which is caused by the mass eccentricity of the outer gimbal and its load.

$$\begin{aligned} \boldsymbol{M}_{\mathrm{o}} &= \begin{bmatrix} M_{\mathrm{ox}} & M_{\mathrm{oy}} & M_{\mathrm{oz}} \end{bmatrix}^{\mathrm{T}} \\ &= m_{\mathrm{o}} \left[\tilde{g}_{\mathrm{o}}\right] \begin{bmatrix} x_{\mathrm{o}} & y_{\mathrm{o}} & z_{\mathrm{o}} \end{bmatrix}^{\mathrm{T}} + m_{\mathrm{m}} \left[\tilde{g}_{\mathrm{o}}\right] \left(\boldsymbol{C}_{\mathrm{o}}^{\mathrm{m}}\right)^{-1} \begin{bmatrix} x_{\mathrm{m}} & y_{\mathrm{m}} & z_{\mathrm{m}} \end{bmatrix}^{\mathrm{T}} \\ &\quad + m_{\mathrm{p}} \left[\tilde{g}_{\mathrm{o}}\right] \left(C_{\mathrm{m}}^{\mathrm{p}} \boldsymbol{C}_{\mathrm{o}}^{\mathrm{m}}\right)^{-1} \begin{bmatrix} x_{\mathrm{p}} & y_{\mathrm{p}} & z_{\mathrm{p}} \end{bmatrix}^{\mathrm{T}} \\ &= \begin{bmatrix} m_{\mathrm{o}} g y_{\mathrm{o}} \cos\alpha - m_{\mathrm{o}} g z_{\mathrm{o}} \sin\alpha + m_{\mathrm{m}} g x_{\mathrm{m}} \cos\alpha \sin\beta + m_{\mathrm{m}} g y_{\mathrm{m}} \cos\alpha \cos\beta - m_{\mathrm{m}} g z_{\mathrm{m}} \sin\alpha \\ \quad + m_{\mathrm{p}} g x_{\mathrm{p}} \cos\alpha \sin\beta \cos\gamma + m_{\mathrm{p}} g x_{\mathrm{p}} \sin\alpha \sin\gamma + m_{\mathrm{p}} g y_{\mathrm{p}} \cos\alpha \cos\beta \\ \quad + m_{\mathrm{p}} g z_{\mathrm{p}} \cos\alpha \sin\beta \sin\gamma - m_{\mathrm{p}} g z_{\mathrm{p}} \sin\alpha \cos\gamma \\ -m_{\mathrm{o}} g x_{\mathrm{o}} \cos\alpha - m_{\mathrm{m}} g x_{\mathrm{m}} \cos\alpha \cos\beta + m_{\mathrm{m}} g y_{\mathrm{m}} \cos\alpha \sin\beta - m_{\mathrm{p}} g x_{\mathrm{p}} \cos\alpha \cos\beta \cos\gamma \\ \quad m_{\mathrm{p}} g y_{\mathrm{p}} \cos\alpha \sin\beta - m_{\mathrm{p}} g z_{\mathrm{p}} \cos\alpha \cos\beta \sin\gamma \\ m_{\mathrm{o}} g x_{\mathrm{o}} \sin\alpha + m_{\mathrm{m}} g x_{\mathrm{m}} \sin\alpha \cos\beta - m_{\mathrm{m}} g y_{\mathrm{m}} \sin\alpha \sin\beta + m_{\mathrm{p}} g x_{\mathrm{p}} \sin\alpha \cos\beta \cos\gamma \\ \quad - m_{\mathrm{p}} g y_{\mathrm{p}} \sin\alpha \sin\beta + m_{\mathrm{p}} g z_{\mathrm{p}} \sin\alpha \cos\beta \sin\gamma \end{bmatrix}, \end{aligned} \tag{10}$$

where $[\tilde{g}_{\mathrm{o}}]$ denotes the anti-symmetric matrix of vector $\boldsymbol{g}_{\mathrm{o}}$ in $o_{\mathrm{o}}x_{\mathrm{o}}y_{\mathrm{o}}z_{\mathrm{o}}$.

Since the outer gimbal can rotate only around x_{o} and the unbalance torque can only be generated along x_{o}, the static balance condition $M_{\mathrm{ox}}=0$ should be met, i.e.

$$\begin{aligned} &m_{\mathrm{o}} g y_{\mathrm{o}} \cos\alpha - m_{\mathrm{o}} g z_{\mathrm{o}} \sin\alpha + m_{\mathrm{m}} g x_{\mathrm{m}} \cos\alpha \sin\beta + m_{\mathrm{m}} g y_{\mathrm{m}} \cos\alpha \cos\beta - m_{\mathrm{m}} g z_{\mathrm{m}} \sin\alpha + m_{\mathrm{p}} g x_{\mathrm{p}} \cos\alpha \sin\beta \cos\gamma \\ &+ m_{\mathrm{p}} g x_{\mathrm{p}} \sin\alpha \sin\gamma + m_{\mathrm{p}} g y_{\mathrm{p}} \cos\alpha \cos\beta + m_{\mathrm{p}} g z_{\mathrm{p}} \cos\alpha \sin\beta \sin\gamma - m_{\mathrm{p}} g z_{\mathrm{p}} \sin\alpha \cos\gamma = 0 \end{aligned}. \tag{11}$$

Since α, β, γ change with time, only the condition of the Eq. (12) is satisfied. Thus, the Eq. (11) can be true.

$$\begin{cases} x_{\mathrm{p}} = 0 \\ z_{\mathrm{p}} = 0 \\ x_{\mathrm{m}} = 0 \\ y_{\mathrm{o}} = 0 \\ m_{\mathrm{m}} y_{\mathrm{m}} + m_{\mathrm{p}} y_{\mathrm{p}} = 0 \\ m_{\mathrm{o}} z_{\mathrm{o}} + m_{\mathrm{m}} z_{\mathrm{m}} = 0 \end{cases}. \tag{12}$$

As the above process shows, for the inertial stabilization platform with three degree of freedom the key to balance the gimbals is designing a counterweight to counteract the static unbalance torque caused by the mass eccentricity, and make the centroid of each gimbal return to its rotation centre. It can be seen from the Eqs. (6), (9) and (12) that the inner gimbal rotates only around y_p, which means that the mass eccentricity of the inner gimbal and its accessory along y_p has no effect on the unbalance torque of the inner gimbal. However, it affects both the middle and outer ones. Since the middle gimbal rotates only around z_m, the

mass eccentricity of the middle gimbal and its accessory along z_m have no effect on the unbalance torque of the inner and middle gimbals, but only of the outer gimbal. In addition, although the inertial stabilization platform has the inner, the middle and the outer gimbals, each gimbal uses an entirely independent servo apparatus. So, whichever of the gimbals is chosen as the unlocked one to test its unbalance while the two other gimbals are locked, the locked gimbals have a little influence on the measured gimbal.

Therefore, the test sequence of the static unbalance for the inertial stabilization platform should follow the order from the inside gimbal to the outside one. The first step is to fix the outer and middle gimbals, and then to measure the inner gimbal unbalance during its vibration within the allowed rotation angle scale. After that, the inner gimbal is counterweighed according to the test result. The second step is to lock the outer gimbal, simultaneously locking the inner gimbal which has been counterweighed, and to measure the middle gimbal unbalance when it is driven to rotate within the allowed rotation angle scale. After that, the middle gimbal is balanced according to the test results. The last step is to fix simultaneously both the inner and middle gimbals, - already counterweighed – and to measure the outer gimbal unbalance when it is driven to rotate within the allowed rotation angle scale. After that, the outer gimbal is counterweighed until reaching a balanced state according to the test result. Since then, the gimbals of the inertial stabilization platform are all counterweighed.

The aforementioned conditions and characteristics of the static balance for the inertial stabilization platform are based on the assumption that the carrier is motionless. When the carrier has an acceleration $\boldsymbol{a}$, first the acceleration $\boldsymbol{a}$ could be transformed from the coordinate $o_g x_g y_g z_g$ to $o_b x_b y_b z_b$, then the same process can be used to analyse it.

3. The dynamical model analysis of the static unbalance test

One of the gimbal axes is chosen as the measured one according to the measurement sequence from the inside to the outside gimbals. It is important to make sure that the measured gimbal axis is parallel with the horizontal shaft of the angular position turntable before driving it to test the static unbalance. And - in order to eliminate disturbances - the other two gimbals should be fixed in a stable state. In this paper, to simplify the model, the measured gimbal is considered to be a disk with the mass m, and with the rotary inertia J. It is assumed that both the measured gimbal axis and the axis of the angular position turntable take the direction to the positive values of X. So, the single disk coordinate system is built as shown in Fig. 3, where C is the mass centre of the disk. O′, O and e are the whirling centre, the geometry centre and the eccentricity of the disk, respectively. The angular velocity of the disk is $\dot{\phi}$, and the torque of the driven motor is denoted by M_{motor}. Then, the differential equation of the single disk motion can be easily formulated by the rotor dynamics model, which is built according to the second Lagrange equations.

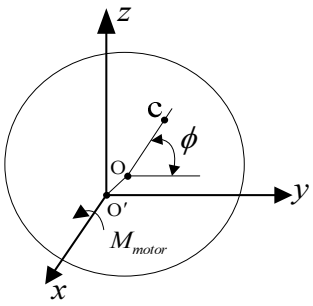

Fig. 3. The single disk coordinate system.

The motion of a rigid body can be separated into the translational and the rotational motions by its centroid. Therefore, the energy of the single disk can be written as follows [20–25]:

$$T = \frac{1}{2}m(\dot{y}^2 + \dot{z}^2 + e^2\dot{\phi}^2 + 2e\dot{\phi}\dot{z}\cos\phi - 2e\dot{\phi}\dot{y}\sin\phi) + \frac{1}{2}(J + me^2)\dot{\phi}^2 . \tag{13}$$

The total virtual work caused by active forces on the single disk system is expressed as

$$\sum W = (M_{motor} - K_f\dot{\phi})\phi - \frac{1}{2}k_{CR}\phi^2 - \frac{1}{2}k(y^2 + z^2) - mg(z + e\sin\phi) - c\dot{y}y - c\dot{z}z , \tag{14}$$

where c is the damping factor of the translational motion, K_f is the damping factor of the rotational motion, k is the bending stiffness of the disk, and K_{CR} is the torsion stiffness of the disk.

According to the Eq. (14), the generalized forces corresponding to ϕ, y, z are shown as follows:

$$\begin{cases} Q_\phi = M_{motor} - K_f\dot{\phi} - k_{CR}\phi - mge\cos\phi \\ Q_y = -ky - c\dot{y} \\ Q_z = -kz - c\dot{z} - mg \end{cases} . \tag{15}$$

Inserting the Eqs. (13) and (14) into the following Second Lagrange Equation[16]:

$$\frac{d}{dt}(\frac{\partial T}{\partial \dot{q}_i}) - \frac{\partial T}{\partial q_i} = Q_i , \tag{16}$$

the final differential equation of the disk motion can be obtained as:

$$\begin{cases} (J + 2me^2)\ddot{\phi} + K_f\dot{\phi} + k_{CR}\phi = M_{motor} - mge\cos\phi + me(\ddot{y}\sin\phi - \ddot{z}\cos\phi) \\ m\ddot{y} + c\dot{y} + ky = me(\ddot{\phi}\sin\phi + \dot{\phi}^2\cos\phi) \\ m\ddot{z} + c\dot{z} + kz = me(\dot{\phi}^2\sin\phi - \ddot{\phi}\cos\phi) - mg \end{cases} . \tag{17}$$

It can be seen from the Eq. (17) that the mass eccentricity not only increases the torsion inertia, but also has an impact on the torsion motion of the disk.

If the line oo' has an angle ψ with respect to the positive values of y, then the projection of the point o can be expressed as $y = |oo'|\cos\psi$, $z = |oo'|\sin\psi$ in the coordinate $yo'z$. In addition, if $|\phi| \le 3^\circ$, then $\sin\phi \approx \phi$, $\cos\phi \approx 1 - 0.5\phi^2$. So, the Eq. (17) can be rewritten by the Eq. (18) to analyse the unbalance torque:

$$(J + 2me^2)\ddot{\phi} + K_f\dot{\phi} + k_{CR}\phi = M_{motor} - mge(1 - 0.5\phi^2) + me|oo'|\sin(\psi - \phi) . \tag{18}$$

Since the disk is an isotropic rigid body, and - what has been discussed in this paper - is a tiny-angle scale vibration, the $|oo'|$ can be regarded as constant. Though the parameters ψ and ϕ are time variables, the difference value between them remains unchanged. Therefore, on the right side of the Eq. (18) the last expression $me|oo'|\sin(\psi - \phi)$ is deemed to be constant.

Integrating both sides of the Eq. (18) by time from t_0 to $t_0 + NT$, the following component can be obtained:

$$\int_{t_0}^{t_0+NT}[(J+2me^2)\ddot{\phi}+K_f\dot{\phi}+k_{CR}\phi-me|oo'|\sin(\psi-\phi)-0.5mge\phi^2]dt+mge\int_{t_0}^{t_0+NT}dt=\int_{t_0}^{t_0+NT}M_{motor}dt\ . \qquad (19)$$

If the disk vibrates with a sinusoidal reciprocating motion within a small angle range the angular velocity is $\dot{\phi}=A\sin(2\pi t/T)$. Then, integrating both sides of the Eq. (18) by time from t_0 to t_0+NT, we obtain exactly N times the vibration period with the amplitude A and the period T for the single disk. Because the integration of a periodic function in its full period is zero, the Eq. (19) can be simplified as follows:

$$mge=\frac{\int_{t_0}^{t_0+NT}M_{motor}dt}{\int_{t_0}^{t_0+NT}dt}\ . \qquad (20)$$

It can be seen from the Eq. (20) that, as long as the disk is doing a stabilized sinusoidal vibration in a small angle range, e.g. from -3° to 3°, the unbalance torque caused by the mass eccentricity can be considered as constant.

In addition, it can be seen from the Eq. (17) that the variation of the static unbalance torque caused by the mass eccentricity is similar to a sinusoid function if the disk rotates in a full circle.

4. The composition of the static unbalance test system

The composition of the static unbalance test system for the inertial stabilization platform is shown in Fig. 4.

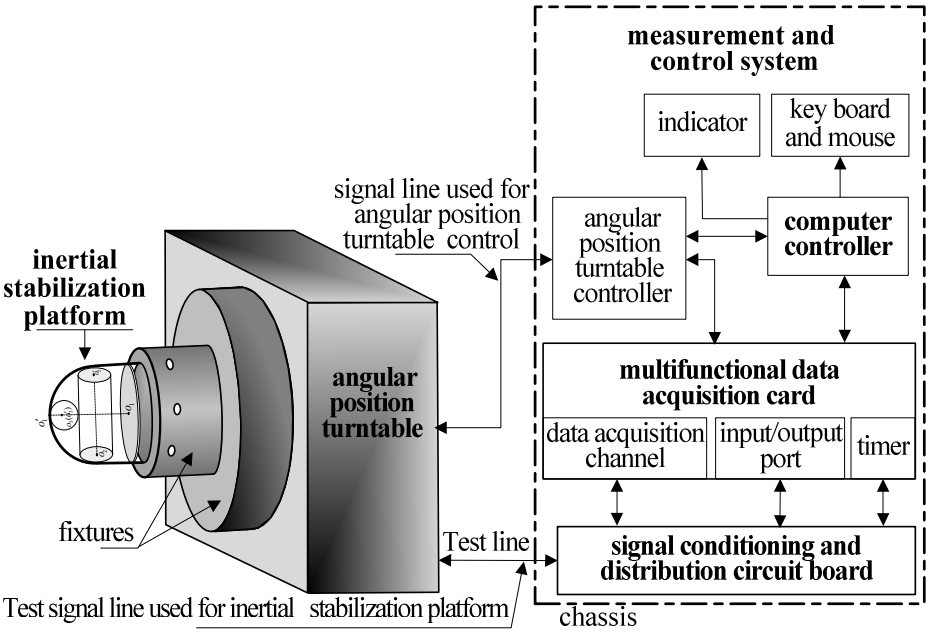

Fig. 4. The composition of the static unbalance test system.

It can be seen that the test system consists of controllers from NI Company, multi-functional data acquisition cards, a self-developed signal conditioning board, a horizontal shaft angular position turntable, various fixtures, a power source, etc.

In the static unbalance test system, the signal conditioning board is not only used to communicate between the measured inertial platform and the multifunction data acquisition card, but also to deal with the signal scale transformations and filtration. The angular position turntable is driven by an AC servo controller, and the control signal is transmitted by a serial port line from the controller of the static unbalance test system. The control signals of the entire gimbal axis come from I/O ports and timers of the multifunction data acquisition card, which is also controlled by the controller.

5. The implementation of the static unbalance test

5.1. The test procedures

The static unbalance test procedures of the measured gimbal axis by the developed measurement system shown in Fig. 4 are introduced as follows.

The first step is to install the measurement system, where the measured gimbal axis of the inertial platform is adjusted paralleling to the horizontal axis of the angular position turntable by changing the orientation of the sectional fixture, and the other two gimbal axes are fixed in a stable state.

The second step is to record the initial zero-locations of the angular position turntable and the measured gimbal axis. The angular position, where the angular position turntable is driven to reach and to be locked, is pre-set.

The third step is to input all the needed parameters to the controller and run the monitoring software which is programmed by the graphical programming software Lab VIEW. So the running status of the system can be displayed directly by animations, graphs, curves and virtual panels on the indicator.

The fourth step is to choose a gimbal axis of the inertial stabilization platform as the measured gimbal according to the sequence of the static unbalance test. At the same time, the other two gimbals must be locked by the dual-loop PID control method.

The fifth step is to drive the angular position turntable to each pre-set angular position θ_i, where i is equal to 1, 2, 3, ⋯, 36 in this paper. Then, the angular position turntable is locked according to the angular displacement control signal which is generated by the test system controller.

The sixth step is to drive the measured gimbal axis to do a limited angle sinusoidal vibration at the angular velocity of $\dot{\phi} = A\sin(2\pi t/T)$. At the same time, the real time drive current of the measured gimbal axis is acquired and recorded.

The seventh step is to obtain the unbalance torque of the measured gimbal axis by the multi-cycle integration of the driven current. According to the analysis of the measured gimbal in Section 2, the expression of the unbalanced value $M_{\theta i}$ can be obtained.

$$M_{\theta i} = K_T \frac{\int_{t_{1i}}^{t_{2i}} i_a dt}{\int_{t_{1i}}^{t_{2i}} dt}, \tag{21}$$

where i_a denotes the driven current of the motor mounted on the measured gimbal, t_{2i} and t_{1i} are the upper and lower time limits of integration for the measured current i_a during the *i*-th measurement.

The eighth step is to repeat the process from the fifth step to the seventh step until the whole test has been done (executed) for every pre-set angular position of the turntable.

5.2. Data processing

Generally, it is difficult to derive the amount and the distribution of the unbalance torque directly from the data and diagrams got from engineering experiments. Therefore, in order to solve this problem and better plot the curve between $M_{\theta i}$ and θ_i, the least squares fitting method is adopted to deal with the 36 group records [27].

The curve between $M_{\theta i}$ and θ_i which is drawn by using the measured data is similar to a sine curve; it just shows the correctness of the foregoing analysis methods. So, the data fitting curve is selected as follows:

$$MT_{\theta i} = MT_s \cdot \sin(\theta_i + b) + MK \,, \tag{22}$$

where the variable θ_i denotes the angular position of the angular position turntable, whereas b and MT_s denote the phase position and the peak value of the unbalanced torque, respectively. MK denotes the disturbance torque, and $MT_{\theta i}$ denotes the fitting value of the unbalance torque while the angular position turntable reaches θ_i.

Inserting the measured data into the Eq. (22) and solving the equation enables to obtain the MT_s, b and MK values.

In order to find out the unbalance position from the figure, at least one period of the variable θ_i should be plotted. A sketch map between $M_{\theta i}$ and θ_i is plotted in Fig. 5 according to the 36 group test data, which have been processed by the least squares fitting method.

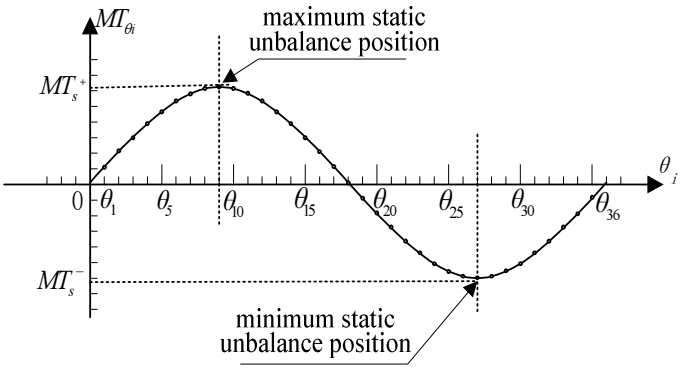

Fig. 5. A sketch map between $M_{\theta i}$ and θ_i.

According to the angular position θ_i found from the fitting graph $MT_s \sim \theta_i$, first the angular position turntable is driven back to its original position, which is marked as the zero point. Presently, the angular position turntable is driven again in the same direction as before until it arrives at the position θ_i. Then the angular position turntable is fixed. If the direction of the angular position turntable is clockwise (or anticlockwise) in the previous measuring process, on the end face of the measured gimbal, the unbalance position should be on the left (or right) side of the horizontal diameter, while the load position should be placed on the right (or left) side. Furthermore, the counterweight can be designed as follows:

$$m = \frac{MT_s}{R \cdot g}, \tag{23}$$

where m denotes the counterweight and R denotes the radius of the measured gimbal axis.

6. The test results and analysis

A simulator of the inertial stabilization platform is designed as shown in Fig. 6, which is used to validate the effectiveness of the proposed method and estimate the precision of the developed system.

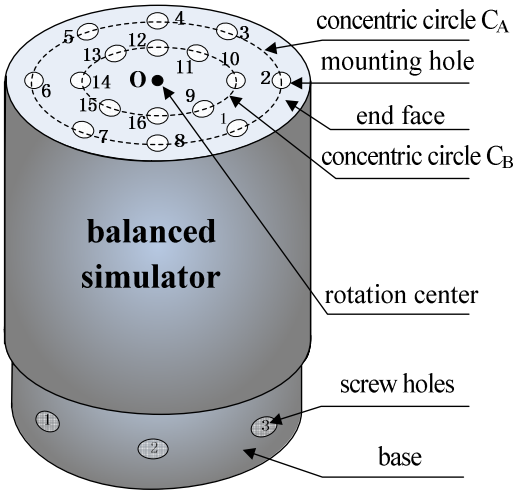

Fig. 6. A sketch map of the balanced simulator.

The simulator has the same hardware configuration and electrical characteristics as the outer gimbal of the inertial stabilization platform, and it is counterweighted and calibrated before the measurement. There are two concentric circles C_A and C_B on the end face of the simulator and their centres are consistent with the end face centre o. The radius of the concentric circle C_A is 5.10 cm, and the C_B one is 3.50 cm. In order to load the clump weight during the measuring procedure, there are 16 mounting holes distributed on the two concentric circles. The 1th to 8th mounting holes are distributed on the circle C_A, and the other 9th to 16th mounting holes are distributed on the concentric circle C_B.

6.1. The loading test

There is a mounting hole on the C_A's radius which is in the direction of $45.50°$ related to the initial zero position. A 25.81 gram mass is imposed on this mounting hole to generate a static unbalance torque of $12.91\ \mathrm{mN \cdot m}$. The angular position turntable is driven to every pre-set position, so the total number of measurements equals to 36. For each angular position, the angular position turntable is locked. After that, the measured gimbal is driven to do a sinusoidal vibration in a small angle range and the angular rate of $\dot{\phi} = 2\sin(0.50\pi t)$. The static unbalance torque $M_{\theta i}$ is calculated from the Eq. (21) using the real time monitor data. The results are listed in Table 1.

Table 1. The test values of the static unbalance torque $M_{\theta i}$ while the turntable reaches θ_i.

i	1	2	3	4	5	6	7	8	9
θ_i [°]	0.00	10.00	20.00	30.00	40.00	50.00	60.00	70.00	80.00
$MT_{\theta i}$ [mN·m]	11.94	13.26	13.85	15.28	15.77	15.89	15.68	14.84	14.27
i	10	11	12	13	14	15	16	17	18
θ_i [°]	90.00	100.0	110.0	120.0	130.0	140.0	150.0	160.0	170.0
$MT_{\theta i}$ [mN·m]	12.91	11.08	9.23	7.13	5.26	2.83	0.53	-1.03	-3.35
i	19	20	21	22	23	24	25	26	27
θ_i [°]	180.00	190.0	200.0	210.0	220.0	230.0	240.0	250.0	260.0
$MT_{\theta i}$ [mN·m]	-5.16	-6.54	-7.96	-8.67	-8.84	-8.80	-8.52	-8.29	-7.20
i	28	29	30	31	32	33	34	35	36
θ_i [°]	270.00	280.0	290.0	300.0	310.0	320.0	330.0	340.0	350.0
$MT_{\theta i}$ [mN·m]	-5.61	-3.67	-2.70	-0.46	1.73	4.25	6.35	7.90	10.24

As previously mentioned in this paper, it is difficult to check the amount and the position of the static unbalance torque from Table 1, so the data are inserted into the Eq. (22), and the fitted result is

$$MT_{\theta i} = 12.04\sin(\theta_i + 44.20) + 3.47\,. \tag{24}$$

According to the fitting formula, i.e. the Eq. (24), the fitted value of the static unbalance torque is 12.04 mN·m, and the fitted phase is 44.20°. So, there is the torque error of -0.87 mN·m between the calculated value and the real (loaded) one. Also, the phase error between the calculated and the really loaded one is $-1.30°$. It confirms a high accuracy of this loading test. The measured and fitted results of the static unbalance torque are $M_{\theta i}$ and $MT_{\theta i}$, respectively. They are plotted in the upper diagram of Fig. 7. The residual errors are shown in the lower diagram; the maximum absolute value of δ is 0.64 mN·m. It is obvious that the results presented in Table 1 and Fig. 7 are satisfactory, which shows a good effectiveness of the method and a high accuracy of the measuring system.

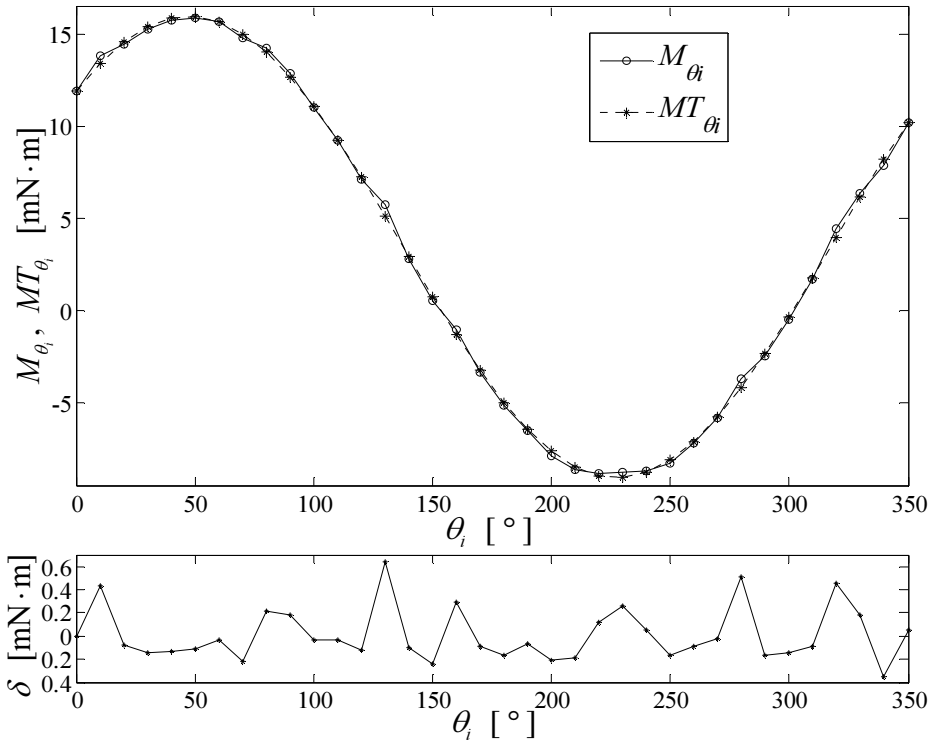

Fig. 7. The measured and fitted curves between $M_{\theta i}$ and θ_i.

Because of the contingency, it is difficult to confirm the effectiveness of the proposed method and to completely estimate the precision of the developed system with a single loading test. So, two groups of loading tests were carried out, and their results are presented in Tables 2 and 3, respectively. In the Tables m_N denotes the loaded mass during the measuring procedure, MT_{LoadN} denotes the generated static unbalance torque by the loaded mass, b_{LoadN} denotes the orientation of the loaded mass. MT_{sN} denotes the test value of the loaded static unbalance torque. b_N denotes the test orientation of the loaded static unbalance torque, δ_{MTN} denotes the residual errors between MT_{sN} and MT_{LoadN}, and δ_{bN} represents the residual errors between b_N and b_{LoadN}.

(1) The first group of loading tests

During each single loading test, a different mass m_N is imposed on the simulator by one of the mounting holes - located on the circle C_A - to generate the static unbalance torque. According to the method proposed in this paper, there are 36 test points in each loading test. The results of 8 loading tests are listed in Table 2.

Table 2. The loading test of the static unbalance torque (The mass is imposed on the circle C_A).

N		1	2	3	4	5	6	7	8
Load value	The radius of the concentric circle C_A is 5.10 cm.								
	m_N [gram]	15.53	20.49	25.81	30.24	35.63	40.16	44.57	50.05
	MT_{LoadN} [mN·m]	7.78	10.25	12.91	15.13	17.83	20.10	22.30	25.04
	b_{LoadN} [°]	270.30	89.50	45.50	224.80	180.50	314.50	135.10	0.20
Tested value	MT_{sN} [mN·m]	9.01	9.13	12.04	14.34	17.15	19.66	22.56	25.12
	b_N [°]	268.46	91.02	44.20	225.85	179.72	313.93	135.58	0.56
Error	δ_{MTN} [mN·m]	+1.23	-1.12	-0.87	-0.79	-0.68	-0.44	+0.26	+0.08
	δ_{bN} [°]	-1.84	+1.52	-1.30	+1.05	-0.78	-0.57	0.48	0.36

It can be seen from Table 2 that the maximum absolute value of δ_{MTN} does not exceed 1.50 mN·m, and the maximum absolute value of δ_{bN} does not exceed $2°$. In this paper, RMSE is calculated and used to evaluate the effectiveness of the method and the accuracy of the measuring system.

$$\mathrm{RMSE}_{MT}=\sqrt{\frac{1}{8}\sum_{N=1}^{8}(MT_{sN}-MT_{LoadN})^2}=0.78\,, \tag{25}$$

$$\mathrm{RMSE}_{b}=\sqrt{\frac{1}{8}\sum_{N=1}^{8}(b_N-b_{LoadN})^2}=1.11\,. \tag{26}$$

Generally, the static unbalance test systems, based on the principle of hydrostatic supporting or optical adjusting, have the static unbalance torque errors no less than 10 mN·m and the orientation errors no less than 20°. The loading test demonstrated the effectiveness and a high accuracy of the measuring system.

(2) The second group of loading tests

For the second group of loading tests, the adopted mass m_N is the same as for the first group of loading tests, but it is imposed on one of the C_B's mounting holes in each single loading test. Like before, the results of eight single loading tests are listed in Table 3.

Table 3. The loading test of the static unbalance torque (The mass is imposed on the circle C_B).

N		9	10	11	12	13	14	15	16
Load value	The radius of the concentric circle C_B is 3.50 cm.								
	m_N [gram]	15.53	20.49	25.81	30.24	35.63	40.16	44.57	50.05
	MT_{LoadN} [mN·m]	5.34	7.03	8.86	10.38	12.24	13.79	15.31	17.18
	b_{LoadN} [°]	270.30	89.50	45.50	224.80	180.50	314.50	135.10	0.20
Tested value	MT_{sN} [mN·m]	7.32	5.37	7.32	11.72	13.25	12.93	15.84	16.93
	b_N [°]	267.39	92.03	47.63	226.75	178.58	313.28	134.23	0.74
Error	δ_{MTN} [mN·m]	+1.98	-1.66	-1.54	+1.34	+1.01	-0.86	+0.53	-0.25
	δ_{bN} [°]	-2.91	+2.53	2.13	+1.95	-1.57	-1.22	-0.87	0.54

The values of RMSE_{MT} and RMSE_b calculated with the Eqs. (25) and (26) are 1.27 mN·m and 1.88°, respectively. Compared with the values obtained in the first group of loading tests, it is obvious that the RMSE values are greater. The reason is that in the second group of loading tests the mass m_N is imposed on the simulator in the mounting holes which are located on the circle C_B, and the radius of C_B is shorter than that of C_A.

In order to find out the change rules for the test errors δ with different loaded masses m_N and their locations, the test errors δ listed in Table 2 and Table 3 are shown as absolute values. Then, their relation is shown in Figs. 8 and 9, respectively.

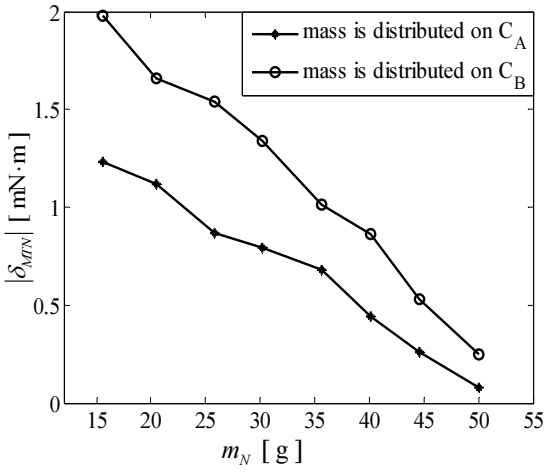

Fig. 8. The relation between δ_{MTN} and m_N.

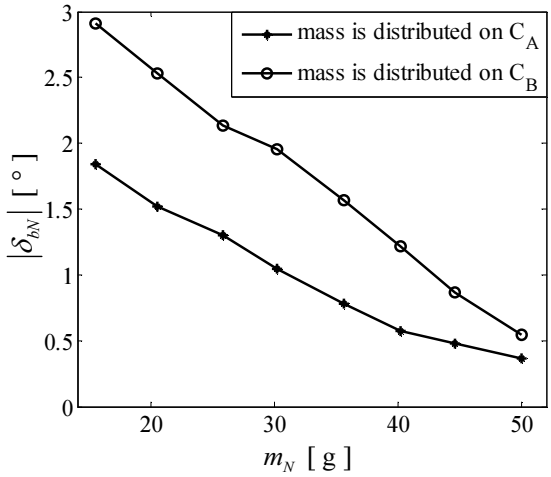

Fig. 9. The relation between δ_{bN} and m_N.

It can be seen from Figs 8 and 9 that - when maintaining the same distance from the rotational centre - the values of δ_{MTN} and δ_{bN} gradually decrease with the increase of the mass m_N which is imposed on the simulator. Similarly, when keeping the mass m_N equal, the obtained values of δ_{MTN} and δ_{bN} are smaller for the mass locations farther from the rotational centre of simulator. This exactly satisfies the regular pattern of the torque.

6.2. The repeatability test

In order to confirm the accuracy and stability of the proposed method, two groups of repeatability tests were carried out. Both the clump weight and mounting hole are pre-selected for every group of repeatability tests. MT_{Load} denotes the generated static unbalance torque by the loaded clump weight, b_{Load} denotes the direction of the loaded clump weight, MT_{si}

represents the test value of the loaded static unbalance torque, b_i represents the test orientation of the loaded static unbalance torque, δ_{MIi} denotes the residual error between MT_{si} and MT_{Load}, and δ_{bi} represents the residual error between b_i and b_{Load}.

(1) The first group of repeatability tests

A mounting hole is located on the C_A circle in the direction of $45.50°$ related to the initial zero position. A 25.81 gram mass is imposed on this mounting hole to generate the static unbalance torque of $12.91\ \mathrm{mN\cdot m}$. According to the method proposed in this paper, there are 36 test points in each repeatability test. Ten repeatability tests are performed. Their results are listed in Table 4.

Table 4. The repeatability test of the static unbalance torque (The number of test points is 36).

i		1	2	3	4	5	6	7	8	9	10
Load value		$b_{Load}=45.50^{\circ}$, $MT_{Load}=12.91\ \mathrm{mN\cdot m}$									
Tested value	b_i [°]	46.69	45.71	43.83	44.80	46.75	44.92	45.34	46.97	45.58	44.89
	MT_{si} [mN·m]	12.07	12.83	13.03	13.76	12.78.	13.15	12.90	12.05	13.21	13.89
Error	δ_{bi} [°]	1.19	0.21	-1.67	-0.70	1.25	-0.58	-0.16	1.47	0.08	-0.61
	δ_{MIi} [mN·m]	-0.84	-0.08	0.12	0.85	-0.13	0.24	-0.01	-0.86	0.30	0.98

During a repeatability test, the RMSE values are used to define the accuracy and stability of the proposed method. They are calculated as follows:

$$\mathrm{RMSE}_{MT}=\sqrt{\frac{1}{10}\sum_{i=1}^{10}(MT_{si}-MT_{Load})^2}=0.58, \tag{27}$$

$$\mathrm{RMSE}_{b}=\sqrt{\frac{1}{10}\sum_{i=1}^{10}(b_i-b_{Load})^2}=0.96. \tag{28}$$

It is obvious that the accuracy and stability of the proposed method are confirmed by the results which are calculated by the Eqs. (27) and (28).

In the first group of repeatability tests the number of test points is equal to 36 during every test. Although the calculated RMSE values are very small, the test process takes a lot of time. According to the theory of least squares fitting, in the case of the test data accuracy, the static unbalance values of MT_s, b and MK are fitted by a finite number or a large number test point data. The difference of fitted results between them should be small. So, the second group of repeatability tests is carried out.

(2) The second group of repeatability tests

During the second group of repeatability tests, the clump weight and mounting holes are the same as in the first group. In order to save the testing time, the number of test points is reduced to 18 during every repeatability test. In the same way, 10 repeatability tests are performed and their results are listed in Table 5.

Table 5. The repeatability test of the static unbalance torque (The number of test points is 18).

i		1	2	3	4	5	6	7	8	9	10
Load value		$b_{Load}=45.50^{\circ}$, $MT_{Load}=12.91$ mN·m									
Tested value	b_i [°]	46.53	46.37	46.55	45.05	47.15	44.88	44.32	45.76	44.87	46.41
	MT_{si} [mN·m]	12.02	11.83	12.71	12.17	14.04	13.86	12.34	11.97	13.49	13.93
Error	δ_{bi} [°]	1.03	0.87	1.05	-0.45	1.65	-0.62	-1.18	0.26	-0.63	0.91
	δ_{MTi} [mN·m]	-0.89	-1.08	-0.20	-0.74	1.13	0.95	-0.57	-0.94	0.58	1.02

Based on the data listed in Table 5, it can be easily calculated with the Eq. (27) and (28), that the value of RMSE_{MT} is 0.86 mN·m, and the value of RMSE_{b} is 0.95°. Compared with the values obtained in the first group of repeatability tests, the RMSE values are a bit higher, but the test process duration is twice shorter. It can be concluded that the precision test value of the static unbalance can be fitted with a small amount of test point data while the measured gimbal axis is controlled to run a good state, and its status data are collected more accurately. This method does not affect the static unbalance test accuracy, but also saves a lot of the testing time.

Both the loading and repeatability tests fully prove that the proposed test method has a good stability, and the developed static unbalance test system has a high testing precision.

7. Conclusions

The static balance condition and measuring sequence for each gimbal axis of the inertial stabilization platform are obtained based on the analysis of the coupling effects caused by the mass eccentricity. After analysing the dynamic model of the measured gimbal axis, a new approach is proposed to test the static unbalance of the gimbal axis. Considering the periodicity of the sine function, the static unbalance can be obtained by a multi-cycle integration of the drive currents which are collected when the measured gimbal axis is driven to do a small angle sinusoidal motion. A measuring system using this test method is also developed. The NI Company multifunction card is used to perform the data acquisition and processing in the developed measuring system, which not only reduces the design complexity of the software and hardware, but also enhances the measurement accuracy. Finally, the accuracy and stability of the method proposed in this study is confirmed by the experimental results.

This paper not only develops a novel method to measure and poise the unbalanced gimbal axis for the inertial stabilization platform, but also provides a new solution for measuring the static unbalance rotor of another assembled machinery. This test method does not cause a contamination of the device under test and also has a high environmental adaptability and a high test speed. Because of the good characteristics, this method will be widely applied in the engineering field.

Acknowledgements

This research is partially supported by the Major State Basic Research Development Program of China (No. 2014CB744200), the National Natural Science Foundation of China (No. 61233005), and the Fundamental Research Funds for the Central Universities, China (No. YWF-10-03-013), and the Specialized Research Fund for the Doctoral Program of Higher Education, China (No. 20101102120041).

References

[1] Hilkert, J. M. (2008). Inertially stabilized platform technology concepts and principles. *Control Systems, IEEE*, 28(1), 26–46.

[2] Nguyen, H. Q. P., Kang, H. J., Suh, Y. S., Elle, O. J. (2012). A platform stabilization algorithm based on feed forward visual-inertial servoing. *International Journal of Precision Engineering and Manufacturing,*13(4), 517─526.

[3] Abdo, M. M., Vali, A. R., Toloei, A. R., Arvan, M. R. (2014). Stabilization loop of a two axes gimbal system using self-tuning PID type fuzzy ontroller. *ISA Transactions*, 53, 591–602.

[4] Ji, W., Li, Q., Xu, B., Zhao, D., Fang, S. X. (2011). Adaptive fuzzy PID composite control with hysteresis-band switching for line of sight stabilization servo system. *Aerospace Science and Technology*, 15, 25─32.

[5] Masten, M. K. (2008). Inertially stabilized platforms for optical imaging systems. *Control Systems, IEEE*, 28(1), 47–64.

[6] Kennedy, P. J., Kennedy, R. L. (2003). Direct versus indirect line of sight (LOS) stabilization. *Control Systems Technology, IEEE Transactions on,* 11(1), 3–15.

[7] Gajda, J., Sroka, R., Żegleń, T. (2007). Accuracy analysis of WIM systems calibrated using pre-weighed vehicles method. *Metrology and Measurement Systems*,14(4), 517–527.

[8] Yu, S., Zhao,Y. Z. (2010). A New Measurement Method for Unbalanced Moments in a Two-axis Gimbaled Seeker. *Chinese Journal of Aeronautics*, 23(1), 117–122.

[9] Kim, K. S. (2002). Eccentricity compensation in optical storage systems: Analysis and experiments. *Japanese journal of applied physics*, 41(10R), 6302.

[10] Kim, S., Ishimoto, T., Nakaoki, A., Kawakubo, O. (2008). Eccentricity Compensation Mechanism for Improving Reliability of Removable Performance in Near-Field Optical Disc Drive System. *Japanese Journal of Applied Physics*, 47(7), 5953–5954.

[11] Ebrahimi, B. M., Etemadrezaei, M., Faiz,J. (2011). Dynamic eccentricity fault diagnosis in round rotor synchronous motors. *Energy Conversion and Management*, 52 (5), 2092–2097.

[12] Penoyer, R. F. (2004). Automatic Torque Balance for Magnetic Anisotropy Measurements. *Review of Scientific Instruments*, 30 (8), 711–714.

[13] Zhou, S., Stephen, Dyer, S. W., Shin, K. K., Shi, J., Ni, J. (2004). Extended Influence Coefficient Method for Rotor Active Balancing During Acceleration. *Journal of Dynamic Systems, Measurement, and Control,* 126(1), 219–223.

[14] Kim, J. S., Lee S. H. (2003). The stability of active balancing control using influence coefficients for a variable rotor system. *International Journal of Advanced Manufacturing Technology*, 22(7-8),562–567.

[15] Moon, J. D., Kim, B. S., Lee, S. H. (2006). Development of the active balancing device for high-speed spindle system using influence coefficients. *International Journal of Machine Tools and Manufacture,* 46 (9), 978–987.

[16] Han, D. J. (2007). Generalized modal balancing for non-isotropic rotor systems. *Mechanical Systems and Signal Processing*, 21(5), 2137–2160.

[17] Deepthikumar, M. B., Sekhar, A. S., Srikanthan, M. R. (2013). Modal balancing of flexible rotors with bow and distributed unbalance. *Journal of Sound and Vibration*, 332(24), 6216–6233.

[18] Xu, B. G., Qu, L. S. (2001). A new practical modal method for rotor balancing. *Proceedings of The Institution of Mechanical Engineers Part C: Journal of Mechanical Engineering Science,* 215(2), 179–189.

[19] Antonov, I. L. (2009). The influence of the inertial properties of the parts of gimbals on the dynamics of a rigid body. *Journal of Applied Mathematics and Mechanics,* 73(6), 631–636.

[20] Chung, J., Ro, D. S. (1999). Dynamic analysis of an automatic dynamic balancer for rotating mechanisms. *Journal of Sound and vibration,* 228(5), 1035–1056.

[21] Zhang, X. L., Wen, B. C., Zhao C. Y. (2014). Vibratory synchronization and coupling dynamic

characteristics of multiple unbalanced rotors on a mass-spring rigid base. *International Journal of Non-Linear Mechanics*, 60, 1–8.

[22] Masry, S. E. (2003). Accuracy of Rotation around an Axis. *Review of Scientific Instruments,* 39(12), 1825–1828.

[23] Lin, Y. L., Chu, F.L. (2010). The dynamic behavior of a rotor system with a slant crack on the shaft. *Mechanical Systems and Signal Processing*, 24 (2), 522–545.

[24] Chasalevris, A., Papadopoulos, C. (2014). A novel semi-analytical method for the dynamics of nonlinear rotor-bearing systems. *Mechanism and Machine Theory,* 72, 39–59.

[25] Santolaria,J., Conte, J., Pueo, M., Javierre, C.(2014). Rotation error modeling and identification for robot kinematic calibration by circle point method. *Metrology and Measurement Systems*, 21(1), 85–98.

[26] Vibet, C. (1995). Dynamics modeling of Lagrangian mechanisms from inertial matrix elements. Computer methods in applied mechanics and engineering, 123(1), 317–326.

[27] Ardeleanu, A., Ramos, P. (2011). Real time PC implementation of power quality monitoring system based on multiharmonic least-squares fitting. *Metrology and Measurement Systems,* 18(4), 543–556.